

LETTER TO THE EDITOR

First detection of the 448 GHz ortho-H₂O line at high redshift: probing the structure of a starburst nucleus at $z = 3.63$

C. Yang (杨辰涛)¹, E. González-Alfonso², A. Omont³, M. Pereira-Santaella⁴, J. Fischer⁵,
A. Beelen⁶, and R. Gavazzi³

¹ European Southern Observatory, Alonso de Córdova 3107, Casilla, 19001 Vitacura, Santiago, Chile
e-mail: cyang@eso.org

² Universidad de Alcalá, Departamento de Física y Matemáticas, Campus Universitario, 28871 Alcalá de Henares, Madrid, Spain

³ Institut d'Astrophysique de Paris, UMR7095 CNRS & Sorbonne Université (UPMC), 98 bis bd Arago, 75014 Paris, France

⁴ Centro de Astrobiología (CSIC-INTA), Ctra. de Ajalvir, Km 4, 28850 Torrejón de Ardoz, Madrid, Spain

⁵ George Mason University, Department of Physics & Astronomy, MS 3F3, 4400 University Drive, Fairfax, VA 22030, USA

⁶ Institut d'Astrophysique Spatiale, CNRS UMR 8617, Université Paris-Sud, Université Paris-Saclay 91405 Orsay, France

Received 14 December 2019 / Accepted 17 January 2020

ABSTRACT

Submillimeter rotational lines of H₂O are a powerful probe in warm gas regions of the interstellar medium (ISM), tracing scales and structures ranging from kiloparsec disks to the most compact and dust-obscured regions of galactic nuclei. The ortho-H₂O(4₂₃ – 3₃₀) line at 448 GHz, which has recently been detected in a local luminous infrared galaxy, offers a unique constraint on the excitation conditions and ISM properties in deeply buried galaxy nuclei because the line requires high far-infrared optical depths to be excited. In this letter, we report the first high-redshift detection of the 448 GHz H₂O(4₂₃ – 3₃₀) line using ALMA in a strongly lensed submillimeter galaxy (SMG) at $z = 3.63$. After correcting for magnification, the luminosity of the 448 GHz H₂O line is $\sim 10^6 L_{\odot}$. In combination with three other previously detected H₂O lines, we build a model that resolves the dusty ISM structure of the SMG, and find that it is composed of a ~ 1 kpc optically thin (optical depth at 100 μm $\tau_{100} \sim 0.3$) disk component with a dust temperature $T_{\text{dust}} \approx 50$ K that emits a total infrared power of $5 \times 10^{12} L_{\odot}$ with a surface density $\Sigma_{\text{IR}} = 4 \times 10^{11} L_{\odot} \text{ kpc}^{-2}$, and a very compact (0.1 kpc) heavily dust-obscured ($\tau_{100} \gtrsim 1$) nuclear core with very warm dust (100 K) and $\Sigma_{\text{IR}} = 8 \times 10^{12} L_{\odot} \text{ kpc}^{-2}$. The H₂O abundance in the core component, $X_{\text{H}_2\text{O}} \sim (0.3\text{--}5) \times 10^{-5}$, is at least one order of magnitude higher than in the disk component. The optically thick core has the characteristic properties of an Eddington-limited starburst, providing evidence that radiation pressure on dust is capable of supporting the ISM in buried nuclei at high redshifts. The multicomponent ISM structure revealed by our models illustrates that dust and molecules such as H₂O are present in regions that are characterized by highly differing conditions and scales, extending from the nucleus to more extended regions of SMGs.

Key words. galaxies: high-redshift – galaxies: ISM – infrared: galaxies – submillimeter: galaxies – radio lines: ISM – ISM: molecules

1. Introduction

Either in the gas phase in warm regions or locked onto dust mantles in cold environments, H₂O is one of the most abundant molecules in the interstellar medium (ISM). In addition to probing a variety of physical processes such as shocks (Flower & Pineau Des Forêts 2010), radiative pumping (González-Alfonso et al. 2008), and outflowing gas (van der Tak et al. 2016), it plays an essential role in the oxygen chemistry of the ISM (e.g., van Dishoeck et al. 2013). Recent observations of the rotational transitions of the H₂O lines in the submillimeter (submm) bands show their ubiquity in infrared (IR) bright galaxies and reveal the tight relation between the submm H₂O lines and dust emission (Yang et al. 2013). Case studies of local IR-bright galaxies have demonstrated that far-IR pumping plays an important role in the excitation of the H₂O lines (e.g., González-Alfonso et al. 2010, 2012; Liu et al. 2017). The H₂O lines offer diagnostics of regions of warm gas, which are usually deeply buried in dust, probing different properties of the ISM than are probed by collisionally excited lines like CO. By modeling the H₂O excitation, dust properties such as the dust temperature, far-IR optical depth, and IR luminosity can be constrained and can even be decomposed

into multiple components that reveal the structure of the dust-obscured ISM (e.g., Falstad et al. 2015).

H₂O lines are a particularly powerful diagnostic tool for studying dusty galaxies. At high redshifts, such galaxies were first discovered in the submm and later characterized as submm galaxies (SMGs, e.g., Smail et al. 1997, or dusty star-forming galaxies, DSFGs, Casey et al. 2014). SMGs are undergoing massive star formation, sometimes reaching the maximum starburst limit (e.g., Barger et al. 2014). The extremely intense star formation suggests that SMGs are in the critical phase of rapid stellar mass assembly. They are likely linked to the local massive spheroidal galaxies (e.g., Toft et al. 2014). However, the nature of SMGs remains debated (e.g., Davé et al. 2010; Narayanan et al. 2015), in part due to the lack of spatially resolved studies of their dusty ISM. Heretofore, most of the H₂O studies at high redshifts have been based on observations with low spatial resolution, which reveal the average properties of the ISM in SMGs (e.g., Omont et al. 2013; Yang et al. 2016). Nevertheless, with ALMA, Calistro Rivera et al. (2018) have reported evidence of significant radial variation of the ISM properties in SMGs and suggested caution when interpreting single band dust continuum data. Furthermore, by measuring the structure

of the dusty ISM, we can assess the stellar mass assembly history of SMGs and build a link to current galaxy populations (e.g., Lang et al. 2019). However, observations like this require resolving the continuum emission in multiple bands that sample the peak of the dust spectral energy distribution (SED) at high frequencies. Moreover, accessing the most dust-obscured regions is observationally challenging. The H_2O lines thus provide an alternative approach to constrain the structure and properties of the dusty ISM in SMGs, owing to their tight link to the far-IR radiation field.

The ortho- $\text{H}_2\text{O}(4_{23} - 3_{30})$ line ($E_u = 433$ K) at 448.001 GHz has recently been detected for the first time in space, with the Atacama Large Millimeter/submillimeter Array (ALMA) in ESO 320-G030, an isolated IR-luminous barred spiral that is likely powered by a starburst because based on X-ray and mid-IR diagnostics, there is no evidence for an obscured active galactic nucleus (AGN; Pereira-Santaella et al. 2017). In this source, $\text{H}_2\text{O}(4_{23} - 3_{30})$ is excited by intense far-IR radiation, rather than being a maser line, as predicted by collisional models (e.g., Neufeld & Melnick 1991; Gray et al. 2016). The spatially resolved observations of the $\text{H}_2\text{O}(4_{23} - 3_{30})$ line and dust continuum in ESO 320-G030 indicate that the line arises from a highly obscured galactic nucleus. Therefore, this highly excited H_2O line is an ideal probe of the deeply buried (optically thick in the far-IR), warm dense nuclear ISM of galaxies.

In this Letter, we report the first high-redshift detection of the ortho- $\text{H}_2\text{O}(4_{23} - 3_{30})$ line in a strongly lensed SMG at $z = 3.63$ in the SMG merging pair G09v1.97. It was first discovered with *Herschel* (Busmann et al. 2013) and was followed up with observation of low spatial resolution of several H_2O and CO lines (Yang et al. 2016, 2017) and a high-resolution observation of the $\text{H}_2\text{O}(2_{11} - 2_{02})$ and CO(6–5) lines (Yang et al. 2019, Y19 hereafter). G09v1.97 has a total molecular gas mass of $10^{11} M_\odot$, and is composed of two gas-rich merging galaxies. The two galaxies, dubbed G09v1.97-R (the receding northern galaxy) and G09v1.97-B (the approaching southern galaxy), are separated by a projected distance of 1.3 kpc ($\sim 0''.2$) and have total intrinsic IR luminosities ($8\text{--}1000 \mu\text{m}$) of 6.3×10^{12} and $4.0 \times 10^{12} L_\odot$, respectively. While both G09v1.97-R and G09v1.97-B are one order of magnitude more powerful than ESO 320-G030 in IR luminosity, like ESO 320-G030, these galaxies are likely powered by star formation, based on their similar line-to-IR luminosity ratios of $L_{\text{CO}(6-5)}/L_{\text{IR}}$ and $L_{\text{H}_2\text{O}(2_{11}-2_{02})}/L_{\text{IR}}$ (Yang et al. 2013, Y19).

We adopt a spatially flat Λ CDM cosmology with $H_0 = 67.8 \text{ km s}^{-1} \text{ Mpc}^{-1}$, $\Omega_M = 0.308$ (Planck Collaboration III 2016), and a Chabrier (2003) initial mass function (IMF) throughout this work.

2. Observations and data reduction

The ALMA observations presented here are part of a dense gas line survey project (ADS/JAO.ALMA#2018.1.00797.S, Yang et al., in prep.). The observations were carried out between December 2018 and January 2019. In this work, we only present data from the Band-3 spectral window covering the ortho- $\text{H}_2\text{O}(4_{23} - 3_{30})$ line centered at 96.137 GHz (observed frequency). Forty-three antennas of the 12 m array were used. The observations were performed under good weather conditions (PWV = 2–5 mm, phase RMS < 9°) with the C43-2 configuration, which provides baselines ranging from 15 to 200 m. J0825+0309 was used as the phase calibrator and J0750+1231 as the bandpass and flux calibrator. A typical ALMA Band-3 calibration uncertainty of 5% is adopted. The total on-source time was 118.4 min, with an additional overhead time of 47.7 min,

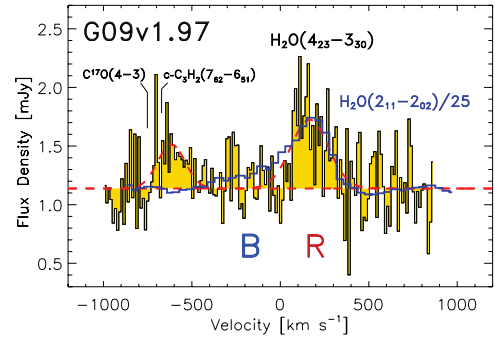


Fig. 1. Spatially integrated spectrum of the 448 GHz H_2O line of G09v1.97 (yellow histograms). *B* and *R* correspond to the blue- and redshifted components of G09v1.97. The overlaid blue line shows the observed $\text{H}_2\text{O}(2_{11} - 2_{02})$ line (Y19) after scaling its flux density down by a factor of 25. The dashed red lines show Gaussian fitting to the emission lines. Close to the 448 GHz H_2O line, we also tentatively detect a 2.3σ emission line (at the velocity of the *R* component) at ~ 449 GHz, which may be either $\text{C}^{17}\text{O}(4-3)$ or $c\text{-C}_3\text{H}_2(7_{62} - 6_{51})$. If the emission is indeed $\text{C}^{17}\text{O}(4-3)$, the integrated flux density ratio of $\text{C}^{16}\text{O}(4-3)/\text{C}^{17}\text{O}(4-3)$ would be ~ 110 , which will be discussed in Yang et al. (in prep.). The dust continuum at rest frame $615 \mu\text{m}$ is also detected with a flux density of $1.13 \pm 0.04 \text{ mJy}$.

resulting in a sensitivity of $\sim 0.12 \text{ mJy beam}^{-1}$ in 50 km s^{-1} velocity bins.

The data were calibrated using the ALMA calibration pipelines with minor flagging. The calibrated data were further processed with imaging and CLEANing using the `tclean` procedure of the CASA software (McMullin et al. 2007) version 5.4.0, with a natural weighting (synthesis beam size of $2.46'' \times 2.03''$ and $\text{PA} = 78.2^\circ$) to maximize the signal-to-noise ratio. The beam size is unable to resolve the source, which has a largest angular structure of $\sim 2''$ (Y19). The spectrum was then extracted from the spatially integrated emission over the entire source (Fig. 1).

3. Analysis and discussion

As shown by the high-angular resolution observations in Y19, the CO(6–5) and $\text{H}_2\text{O}(2_{11} - 2_{02})$ lines of G09v1.97 both mainly consist of *B* and *R* components (which are blueshifted and redshifted, respectively, compared to the system velocity of G09v1.97), with line widths of $\sim 300 \text{ km s}^{-1}$ (Fig. 1). The *B* component originates exclusively from the approaching galaxy G09v1.97-B, while the *R* component arises from the receding galaxy G09v1.97-R. Therefore, the contribution to the spectrum from each merger companion can be distinguished without spatially resolved observations. The lensing magnification for the line varies from ~ 5 to ~ 22 as a function of velocity from the blueshifted to the redshifted velocity components, due to a velocity gradient from south to north (Y19). As a result, *R* is a factor of ≥ 4 brighter than *B* in the spectrum, causing an extremely asymmetric line profile (blue histogram in Fig. 1). The 448 GHz H_2O line is detected with $\geq 5\sigma$ significance, but only in the redshifted component (Fig. 1), namely only in G09v1.97-R. Assuming a similar flux ratio of $\text{H}_2\text{O}(4_{23} - 3_{30})/\text{H}_2\text{O}(2_{11} - 2_{02})$ in *R* and *B*, the 448 GHz H_2O line in G09v1.97-B is thus buried below the noise level. Therefore, we associate the detected 448 GHz H_2O line only with G09v1.97-R. We therefore corrected the lensing magnification for the H_2O line fluxes of G09v1.97-R, as listed in Table 1. The table also includes the observational results on the $\text{H}_2\text{O}(3_{21} - 3_{12})$ (Yang et al. 2016) and $\text{H}_2\text{O}(4_{22} - 4_{13})$ lines (Yang 2017) for G09v1.97-R, which were obtained with

Table 1. Spatially integrated H₂O line properties of G09v1.97-R.

Line	E_u (K)	ν_{rest} (GHz)	$\mu_{\text{R-line}} I_{\text{H}_2\text{O}}$ (Jy km s ⁻¹)	ΔV_{line} (km s ⁻¹)	$\mu_{\text{R-line}} L_{\text{Line}}$ (10 ⁸ L_{\odot})	$\mu_{\text{R-line}} L'_{\text{Line}}$ (10 ¹⁰ K km s ⁻¹ pc ²)	Reference
para-H ₂ O(2 ₁₁ – 2 ₀₂)	137	752.033	4.2 ± 0.6 ^(a)	257 ± 27 ^(b)	7.6 ± 0.4	5.6 ± 0.3	Y16, Y19
ortho-H ₂ O(3 ₂₁ – 3 ₁₂)	305	1162.912	3.7 ± 0.4	234 ± 34	10.3 ± 1.1	2.1 ± 0.2	Y16
para-H ₂ O(4 ₂₃ – 3 ₃₀)	433	448.001	0.16 ± 0.03	250 ^(c)	0.17 ± 0.03	0.60 ± 0.11	This work
ortho-H ₂ O(4 ₂₂ – 4 ₁₃)	454	1207.639	1.8 ± 0.6	328 ± 139	5.2 ± 1.7	0.9 ± 0.3	Y17

Notes. Observed H₂O line properties of G09v1.97-R. We adopt $\mu_{\text{R-line}} = 20$ for the magnification of the velocity-integrated line fluxes of G09v1.97-R (Y19). ^(a)Here, we include an additional 15% uncertainty considering the possible contamination from the interacting region (Y19). ^(b)The value is taken from the NOEMA detection by Yang et al. (2016) of the redshifted component for consistency in the comparison with the other lines detected here, which are also dominated by the redshifted component (G09v1.97-R). ^(c)Here, we adopt a fixed line width for G09v1.97-R of 250 km s⁻¹, according to Yang et al. (2016). **References.** Y16=Yang et al. (2016); Y17=Yang (2017); Y19=Yang et al. (2019).

NOEMA with a similar spatial resolution of $\gtrsim 2''$ (unresolved). The continuum measurements, which are used below to model the H₂O emission, were also corrected to account for G09v1.97-R alone. The limited spatial resolution of the currently highest spatial resolution dust continuum images (Y19) does not allow us to distinguish the fluxes from the merger companions. Nevertheless, the relative contribution by G09v1.97-R can be approximated using the tight correlation between $L_{\text{CO}(6-5)}$ and L_{IR} (Liu et al. 2015; Yang et al. 2017). Because the intrinsic line fluxes from R are about 50% of the total and the magnifications R and B are $\mu_{\text{R}} \approx 20$ and $\mu_{\text{B}} \approx 5$, respectively (Y19), the intrinsic continuum flux densities from G09v1.97-R are a factor ≈ 25 lower than the observed values integrated over the entire G09v1.97 system. We here therefore scaled the measured continuum fluxes down by a factor of 25 and include an uncertainty of 20% associated with the flux scaling.

In G09v1.97-R, the 448 GHz ortho-H₂O(4₂₃ – 3₃₀) line has a luminosity of $8.5 \times 10^5 L_{\odot}$, which is a fraction of 10^{-7} of the total IR luminosity. In addition to the 448 GHz H₂O line, three additional lines of H₂O have previously been detected in G09v1.97-R (Fig. 2 and Table 1): the ortho-H₂O(3₂₁ – 3₁₂), the para-H₂O(2₁₁ – 2₀₂), and the para-H₂O(4₂₂ – 4₁₃) transitions. Interestingly, the 4₂₃ – 3₃₀ and 4₂₂ – 4₁₃ transitions have $J_{\text{upper}} = 4$ levels with very similar energies (425 K versus 433 K), but their A-Einstein coefficients for spontaneous emission differ by a factor of ≈ 500 : 5.4×10^{-5} and 2.8×10^{-2} s⁻¹, respectively (Pickett et al. 1998). Assuming that the upper-level populations of both lines do not strongly differ from the ortho-to-para ratio of 3 appropriate for warm regions, their flux ratio (in Jy km s⁻¹) in optically thin conditions should be $F(1208 \text{ GHz})/F(448 \text{ GHz}) \sim A_{ul}(1208 \text{ GHz})/(3A_{ul}(448 \text{ GHz})) \sim 170$. The observed flux ratio in G09v1.97-R is only ≈ 11 (Table 1), similar to the value of ≈ 15 found in ESO 320-G030 (González-Alfonso et al., in prep.), indicating that the ortho-H₂O(4₂₂ – 4₁₃) line is strongly saturated in both sources. Similar to the situation found in buried nuclei of local (ultra)-luminous IR galaxies ((U)LIRGs), high radiation and column densities in a nuclear component are required to pump the $J_{\text{upper}} = 4$ levels and to account for the corresponding strong H₂O emission from G09v1.97-R.

To estimate the physical conditions and structure of the ISM in G09v1.97-R from the observed H₂O and dust continuum emission, a library of model components was developed following the method described in González-Alfonso et al. (2014). We assumed for each component a spherically symmetric source with uniform physical properties: the dust temperature T_{dust} , the continuum optical depth at 100 μm along a radial path τ_{100} , the column density of H₂O along a radial path $N_{\text{H}_2\text{O}}$, the H₂ density n_{H_2} , the velocity dispersion ΔV , and the gas temperature

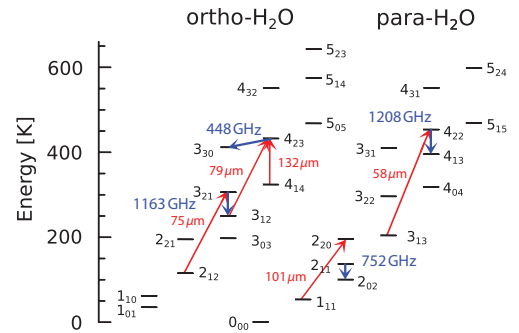


Fig. 2. Energy level diagram of the main para- and ortho-H₂O transitions. Blue arrows indicate the emission lines modeled in this work. Red arrows show the transitions responsible for the associated radiative pumping. The frequencies of the lines and the wavelengths of the far-IR photons are labeled.

T_{gas} . The physical parameters modified from model to model are T_{dust} , τ_{100} , $N_{\text{H}_2\text{O}}$, and n_{H_2} , and we kept $\Delta V = 100$ km s⁻¹ and $T_{\text{gas}} = 150$ K fixed (consistent with the results from CO excitation, Yang et al. 2017). The model components were classified into groups according to their physical parameters, each group covering a regular grid in the parameter space (T_{dust} , τ_{100} , $N_{\text{H}_2\text{O}}$, and n_{H_2}). After we created the model components, all available H₂O line fluxes and continuum flux densities were fit simultaneously using a number N_{C} of model components (up to two components per group) and checking all possible combinations among them. Because the intrinsic line and continuum fluxes (in Jy km s⁻¹ and Jy, respectively) scale as $(1+z)(R/D_L)^2$, where R is the source radius and $D_L = 32.7$ Gpc is the luminosity distance, a χ^2 minimization procedure was used to determine the source radius R of each component for all combinations of model components. Our best model fit corresponds to the combination that yields the lowest χ^2 , while the results for all combinations enable us to calculate the likelihood distribution of the free physical parameters (e.g., Ward et al. 2003), i.e., T_{dust} , τ_{100} , $N_{\text{H}_2\text{O}}$, and n_{H_2} , for each component. The derived parameters (R , the H₂O abundance relative to H nuclei $X_{\text{H}_2\text{O}}$, and L_{IR}) can also be inferred. More details will be given in González-Alfonso et al. (in prep.).

We first attempted to fit the H₂O and continuum emission with a single-model component ($N_{\text{C}} = 1$), but results were unreliable, with a best reduced chi-square value $\chi_{\text{red}}^2 \approx 4$. This was indeed expected because the low-lying H₂O $J_{\text{upper}} = 2-3$ lines are expected to arise in more extended regions than the $J_{\text{upper}} = 4$ lines that trace buried regions (e.g., González-Alfonso et al. 2014; Pereira-Santaella et al. 2017). A better fit was found

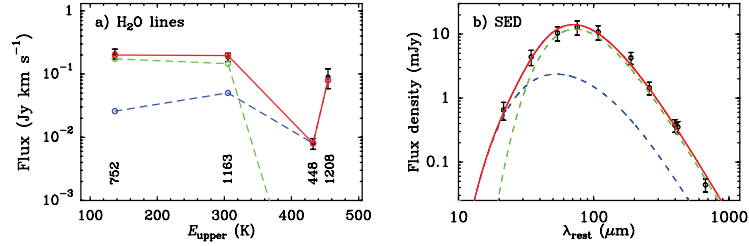


Fig. 3. Best-fit two-component model of G09v1.97-R for (a) the H₂O lines and (b) the dust continuum (colored symbols and lines) compared with observations (black symbols with error bars). Predictions for the two individual ISM components are displayed with dashed green (the disk component) and blue lines (the core component); the total is shown in red. The physical parameters adopted from this model are indicated with arrows in Fig. 4. *Panel a:* numbers indicate the rest frequencies of the lines in GHz. The observed H₂O fluxes and continuum flux densities have been corrected for magnification. The continuum fluxes have also been corrected to only account for the contribution by G09v1.97-R, as described in Sect. 2 (see also Y19).

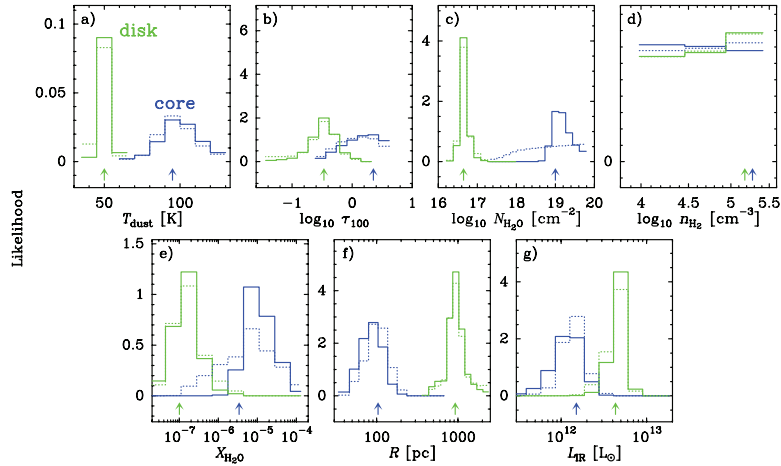


Fig. 4. Solid histograms indicate the likelihood distributions for the physical parameters of the two-component model (green and blue for the disk and core component, respectively). (a)–(d) are fitted parameters while (e)–(g) are derived parameters. Dotted histograms show the likelihood distributions of a fit that ignores the 448 GHz H₂O line, showing consistent results but a high uncertainty in $N_{\text{H}_2\text{O}}$ and $X_{\text{H}_2\text{O}}$. The arrows indicate the values of the best model fit, with results for the H₂O fluxes and continuum flux densities displayed in Fig. 3.

with $N_C = 2$ components (Fig. 3), with $\chi_{\text{red}}^2 \approx 0.9$. In Fig. 4, the arrows indicate the best-fit values, and solid histograms show their likelihood distributions. We find that the $J_{\text{upper}} = 4$ lines are formed in a very warm nuclear region (core) with size $R \sim 100$ pc and $T_{\text{dust}} \sim 100$ K, which is most probably optically thick at far-IR wavelengths ($\tau_{100} \gtrsim 1$). This nuclear core has a luminosity of $L_{\text{IR}} \sim 10^{12} L_{\odot}$, resulting in an extreme IR luminosity surface density $\Sigma_{\text{IR}} = 8 \times 10^{12} L_{\odot} \text{ kpc}^{-2}$. This translates into a surface star formation rate of $\sim 1.1 \times 10^3 M_{\odot} \text{ yr}^{-1} \text{ kpc}^{-2}$ if the contribution to L_{IR} by a possible obscured AGN is negligible because no strong evidence of the presence of an AGN has been found (Yang et al. 2016). A high column density of water, $N_{\text{H}_2\text{O}} \sim 10^{19} \text{ cm}^{-2}$ ($X_{\text{H}_2\text{O}} \sim 10^{-5}$), is found in this core component, which is more than one order of magnitude higher than in the $z=3.9$ quasar host galaxy APM08279+5255 (van der Werf et al. 2011). In addition, the $J_{\text{upper}} = 2$ –3 lines, pumped by absorption of dust-emitted 100 and 75 μm photons (Fig. 2), require an optically thin ($\tau_{100} \sim 0.3$) and more extended region of radius ~ 1 kpc (the disk component), remarkably similar to the projected half-light effective radius traced by the CO(6–5) and H₂O(2₁₁–2₀₂) line emission (0.8 kpc, Y19), and also to the size of the averaged 870 μm dust continuum of SMGs (~ 1 kpc, Gullberg et al. 2019). With $T_{\text{dust}} \sim 50$ K, the disk component dominates the luminosity with $L_{\text{IR}} \sim 5 \times 10^{12} L_{\odot}$ and $\Sigma_{\text{IR}} = 4 \times 10^{11} L_{\odot} \text{ kpc}^{-2}$ (corresponding to $\sim 60 M_{\odot} \text{ yr}^{-1} \text{ kpc}^{-2}$), and has a lower column density and abundance of water than the core, with $N_{\text{H}_2\text{O}} \sim 10^{16} \text{ cm}^{-2}$ ($X_{\text{H}_2\text{O}} \sim 10^{-7}$).

While the effect of the cosmic microwave background (CMB) on the dust SED is included in Fig. 3b following da Cunha et al. (2013) (see also Zhang et al. 2016), the correction is small as $T_{\text{dust}} \gg T_{\text{CMB}} = 12.5$ K. The excitation of H₂O by the CMB, however, is not included in our models, but we verified that for our best-fit model (Fig. 3a), it has a negligible effect on the excitation and flux of the observed lines. A more important source of uncertainty is that our models do not include the effects of spatially varying T_{dust} that are expected in regions that are optically thick in the far-IR (González-Alfonso & Sakamoto 2019). An increasing T_{dust} outside-in would facilitate the H₂O excitation within the core component, and would thus decrease the inferred $N_{\text{H}_2\text{O}}$ to some extent. This effect becomes most relevant for extremely buried sources with N_{H_2} approaching 10^{25} cm^{-2} ($\tau_{100} \gtrsim 10$), which is not excluded for the nuclear core of G09v1.97-R (Fig. 4b).

What is the role of the 448 GHz H₂O line in constraining the model? The dotted histograms in Fig. 4 show that if the 448 GHz H₂O line is excluded, the likelihood distributions of the physical parameters remain similar, but show a less informative distribution for $N_{\text{H}_2\text{O}}$ (and $X_{\text{H}_2\text{O}}$). In this case, the parameters of the nucleus are determined by the 1208 GHz H₂O line, which is optically thick ($\tau_{1208\text{-H}_2\text{O}} = 27.5$). The detection of the more optically thin 448 GHz H₂O line ($\tau_{448\text{-H}_2\text{O}} = 1.0$) confirms the occurrence of the warm nuclear region and enables a significantly more accurate estimate of its $N_{\text{H}_2\text{O}}$ (and $X_{\text{H}_2\text{O}}$). On the other hand, the flat distributions of n_{H_2} in both regions

indicate that the excitation of these H₂O lines is insensitive to n_{H_2} .

Our models, which fit the H₂O line and dust continuum fluxes simultaneously, are sensitive to $N_{\text{H}_2\text{O}}$ and τ_{100} . These two parameters, treated as independent, are linked as $X_{\text{H}_2\text{O}} = N_{\text{H}_2\text{O}} / (1.3 \times 10^{24} \tau_{100} (GDR/100))$, where GDR is the gas-to-dust ratio by mass. For the core component, our best fit yields $N_{\text{H}_2\text{O}}/\tau_{100} \sim 5 \times 10^{18} \text{ cm}^{-2}$. With the assumption of a $GDR = 100$, we obtain $X_{\text{H}_2\text{O}} \sim (0.3\text{--}5) \times 10^{-5}$ (90% confidence interval, Fig. 4e), similar to the abundance in buried galactic nuclei of local (U)LIRGs (González-Alfonso et al. 2012). The similarity of the $N_{\text{H}_2\text{O}}/\tau_{100}$ ratio in the nuclear cores of SMGs and of local (U)LIRGs appears to indicate a fundamental similarity of the gas metallicity to dust ratio in buried galactic nuclei throughout cosmic times.

With the H₂O excitation models, we are able to resolve two distinct components with significantly different properties (e.g., T_{dust} and τ_{100}). These differences reveal the complexity of the ISM structure in SMGs and suggest caution when deriving the physical properties from spatially unresolved observations. For example, an increase in dust temperature and optical depth toward the nuclear region can significantly alter the calculation of size and mass of the ISM dust (e.g., Miettinen et al. 2017; Calistro Rivera et al. 2018). While the value of the star formation rate surface density of the disk component, which dominates the total IR emission, is typical of SMGs (Hodge et al. 2013), the nuclear core shows more extreme conditions. The properties of the optically thick core show excellent agreement with the characteristic L_{IR} surface density ($\sim 10^{13} L_{\odot} \text{ kpc}^{-2}$) and dust temperature (~ 90 K) of Eddington-limited starburst models (Thompson et al. 2005), indicating the importance of radiation pressure on dust in regulating the ISM in the inner 100 pc region of G09v1.97-R. Although we cannot rule out a contribution to the far-IR from an obscured AGN, in addition to the arguments disfavoring a dominant AGN power source discussed in the introduction and in Y19, we also find no strong evidence for the presence of a powerful AGN in G09v1.97-R by checking the q parameter (Condon 1992) and mid-IR excess (see discussions in Yang et al. 2016). This strengthens the case for Eddington-limited starbursts. Nevertheless, further observations are needed to quantify the contribution from an AGN.

4. Conclusions

We reported the first detection of the 448 GHz ortho-H₂O(4₂₃ – 3₃₀) line at high redshift in the $z = 3.63$ lensed submillimeter galaxy G09v1.97-R. In combination with three other transitions of H₂O and dust emission, we have built a radiative transfer model for the H₂O excitation and dust emission. The model decomposes the dust continuum of the SMG into two components, a ~ 1 kpc optically thin ($\tau_{100} \sim 0.3$) disk component with $T_{\text{dust}} = 50$ K emitting a total IR luminosity of $\sim 5 \times 10^{12} L_{\odot}$, and a ~ 0.1 kpc heavily dust-obscured ($\tau_{100} \gtrsim 1$) nuclear core with very warm dust (100 K) and an IR luminosity of $\sim 10^{12} L_{\odot}$. The water abundance in the core ($X_{\text{H}_2\text{O}} \sim 5 \times 10^{-6}$) is more than one order of magnitude higher than in the more extended disk. The surface star formation rate of the core component is $\Sigma_{\text{SFR}} = 1.1 \times 10^3 M_{\odot} \text{ yr}^{-1} \text{ kpc}^{-2}$, which is ~ 20 times higher than that of the disk. The ISM properties of the nucleus of G09v1.97-R resemble the characteristic conditions of an Eddington-limited starburst, indicating that radiation pressure on dust plays an essential role in supporting the ISM.

The optically thin 448 GHz H₂O line is a powerful tool for the study of SMGs around redshift 2–4 (with ALMA Bands

3 and 4). The multicomponent structure derived from the H₂O excitation model reveals the complex nature and morphology of SMGs and may offer clues about the evolutionary link of the SMGs to massive elliptical galaxies today, once high-resolution near-infrared observations of the stellar component are possible and become available with telescopes such as the *James Webb* Space Telescope, JWST.

Acknowledgements. We thank the anonymous referee for very helpful suggestions. C.Y. acknowledges support from an ESO Fellowship. E.G.-A. is a Research Associate at the Harvard-Smithsonian Center for Astrophysics, and thanks the Spanish Ministerio de Economía y Competitividad for support under project ESP2017-86582-C4-1-R. E.G.-A. also thanks the support from the ESO Chile Scientific Visitor Programme. M.P.S. acknowledges support from the Comunidad de Madrid through Atracción de Talento Investigador Grant 2018-T1/TIC-11035. This paper makes use of the following ALMA data: ADS/JAO.ALMA#2018.1.00797.S. ALMA is a partnership of ESO (representing its member states), NSF (USA) and NINS (Japan), together with NRC (Canada), MOST and ASIAA (Taiwan), and KASI (Republic of Korea), in cooperation with the Republic of Chile. The Joint ALMA Observatory is operated by ESO, AUI/NRAO and NAOJ.

References

- Barger, A. J., Cowie, L. L., Chen, C.-C., et al. 2014, *ApJ*, 784, 9
 Bussmann, R. S., Pérez-Fournon, I., Amber, S., et al. 2013, *ApJ*, 779, 25
 Calistro Rivera, G., Hodge, J. A., Smail, I., et al. 2018, *ApJ*, 863, 56
 Casey, C. M., Narayanan, D., & Cooray, A. 2014, *Phys. Rep.*, 541, 45
 Chabrier, G. 2003, *PASP*, 115, 763
 Condon, J. J. 1992, *ARA&A*, 30, 575
 da Cunha, E., Groves, B., Walter, F., et al. 2013, *ApJ*, 766, 13
 Davé, R., Finlator, K., Oppenheimer, B. D., et al. 2010, *MNRAS*, 404, 1355
 Falstad, N., González-Alfonso, E., Aalto, S., et al. 2015, *A&A*, 580, A52
 Flower, D. R., & Pineau Des Forêts, G. 2010, *MNRAS*, 406, 1745
 González-Alfonso, E., & Sakamoto, K. 2019, *ApJ*, 882, 153
 González-Alfonso, E., Smith, H. A., Ashby, M. L. N., et al. 2008, *ApJ*, 675, 303
 González-Alfonso, E., Fischer, J., Isaak, K., et al. 2010, *A&A*, 518, L43
 González-Alfonso, E., Fischer, J., Graciá-Carpio, J., et al. 2012, *A&A*, 541, A4
 González-Alfonso, E., Fischer, J., Aalto, S., & Falstad, N. 2014, *A&A*, 567, A91
 Gray, M. D., Baudry, A., Richards, A. M. S., et al. 2016, *MNRAS*, 456, 374
 Gullberg, B., Smail, I., Swinbank, A. M., et al. 2019, *MNRAS*, 490, 4956
 Hodge, J. A., Karim, A., Smail, I., et al. 2013, *ApJ*, 768, 91
 Lang, P., Schinnerer, E., Smail, I., et al. 2019, *ApJ*, 879, 54
 Liu, D., Gao, Y., Isaak, K., et al. 2015, *ApJ*, 810, L14
 Liu, L., Weiß, A., Perez-Beaupuits, J. P., et al. 2017, *ApJ*, 846, 5
 McMullin, J. P., Waters, B., Schiebel, D., Young, W., & Golap, K. 2007, in *Astronomical Data Analysis Software and Systems XVI*, eds. R. A. Shaw, F. Hill, & D. J. Bell, *ASP Conf. Ser.*, 376, 127
 Miettinen, O., Novak, M., Smolčić, V., et al. 2017, *A&A*, 602, A54
 Narayanan, D., Turk, M., Feldmann, R., et al. 2015, *Nature*, 525, 496
 Neufeld, D. A., & Melnick, G. J. 1991, *ApJ*, 368, 215
 Omont, A., Yang, C., Cox, P., et al. 2013, *A&A*, 551, A115
 Pereira-Santaella, M., González-Alfonso, E., Usero, A., et al. 2017, *A&A*, 601, L3
 Pickett, H. M., Poynter, R. L., Cohen, E. A., et al. 1998, *J. Quant. Spectr. Rad. Transf.*, 60, 883
 Planck Collaboration III. 2016, *A&A*, 594, A13
 Smail, I., Ivison, R. J., & Blain, A. W. 1997, *ApJ*, 490, L5
 Thompson, T. A., Quataert, E., & Murray, N. 2005, *ApJ*, 630, 167
 Toft, S., Smolčić, V., Magnelli, B., et al. 2014, *ApJ*, 782, 68
 van der Tak, F. F. S., Weiß, A., Liu, L., & Güsten, R. 2016, *A&A*, 593, A43
 van der Werf, P. P., Berciano Alba, A., Spaans, M., et al. 2011, *ApJ*, 741, L38
 van Dishoeck, E. F., Herbst, E., & Neufeld, D. A. 2013, *Chemical Reviews*, 113, 9043
 Ward, J. S., Zmuidzinas, J., Harris, A. I., & Isaak, K. G. 2003, *ApJ*, 587, 171
 Yang, C. 2017, Ph.D. Thesis, Paris-Sud, Université Paris-Saclay, France
 Yang, C., Gao, Y., Omont, A., et al. 2013, *ApJ*, 771, L24
 Yang, C., Omont, A., Beelen, A., et al. 2016, *A&A*, 595, A80
 Yang, C., Omont, A., Beelen, A., et al. 2017, *A&A*, 608, A144
 Yang, C., Gavazzi, R., Beelen, A., et al. 2019, *A&A*, 624, A138
 Zhang, Z.-Y., Papadopoulos, P. P., Ivison, R. J., et al. 2016, *R. Soc. Open Sci.*, 3, 160025